Prepared for submission to JCAP

Time-dependent search for neutrino emission from x-ray binaries with the ANTARES telescope

A. Albert[1] M. André[2] G. Anton[3] M. Ardid[4] J.-J. Aubert[5] T. Avgitas[6] B. Baret[6] J. Barrios-Martí[7] S. Basa[8] V. Bertin[5] S. Biagi[9] R. Bormuth[10,11] M.C. Bouwhuis[10] R. Bruijn[10,12] J. Brunner[5] J. Busto[5] A. Capone[13,14] L. Caramete[15] J. Carr[5] S. Celli[13,14,40] T. Chiarusi[16] M. Circella[17] A. Coleiro[6] R. Coniglione[9] H. Costantini[5] P. Coyle[5] A. Creusot[6] A. Deschamps[18] G. De Bonis[13,14] C. Distefano[9] I. Di Palma[13,14] C. Donzaud[6,19] D. Dornic[5] D. Drouhin[1] T. Eberl[3] I. El Bojaddaini[20] D. Elsässer[21] A. Enzenhöfer[5] I. Felis[4] L.A. Fusco[16,22] S. Galatà[6] P. Gay[23,6] S. Geißelsöder[3] K. Geyer[3] V. Giordano[24] A. Gleixner[3] H. Glotin[25,39] R. Gracia-Ruiz[6] K. Graf[3] S. Hallmann[3] H. van Haren[26] A.J. Heijboer[10] Y. Hello[18] J.J. Hernández-Rey[7] J. Hößl[3] J. Hofestädt[3] C. Hugon[27,28] G. Illuminati[13,14,7] C.W. James[3] M. de Jong[10,11] M. Jongen[10] M. Kadler[21] O. Kalekin[3] U. Katz[3] D. Kießling[3] A. Kouchner[6,39] M. Kreter[21] I. Kreykenbohm[29] V. Kulikovskiy[5,30] C. Lachaud[6] R. Lahmann[3] D. Lefèvre[31] E. Leonora[24,32] S. Loucatos[33,6] M. Marcelin[8] A. Margiotta[16,22] A. Marinelli[34,35] J.A. Martínez-Mora[4] A. Mathieu[5] K. Melis[10,12] T. Michael[10] P. Migliozzi[36] A. Moussa[20] C. Mueller[21] E. Nezri[8] G.E. Păvălaș[15] C. Pellegrino[16,22] C. Perrina[13,14] P. Piattelli[9] V. Popa[15] T. Pradier[37] C. Racca[1] G. Riccobene[9] K. Roensch[3] M. Saldaña[4] D. F. E. Samtleben[10,11] A. Sánchez-Losa[7,17] M. Sanguineti[27,28] P. Sapienza[9] J. Schnabel[3] F. Schüssler[33] T. Seitz[3] C. Sieger[3] M. Spurio[16,22] Th. Stolarczyk[33] M. Taiuti[27,28] A. Trovato[9] M. Tselengidou[3] D. Turpin[5] C. Tönnis[7] B. Vallage[33,6] C. Vallée[5] V. Van Elewyck[6] D. Vivolo[36,38] S. Wagner[3] J. Wilms[29] J.D. Zornoza[7] J. Zúñiga[7]

arXiv:1609.07372v1 [astro-ph.HE] 23 Sep 2016

[1]GRPHE - Université de Haute Alsace - Institut universitaire de technologie de Colmar, 34 rue du Grillenbreit BP 50568 - 68008 Colmar, France

[2]Technical University of Catalonia, Laboratory of Applied Bioacoustics, Rambla Exposició,08800 Vilanova i la Geltrú,Barcelona, Spain

[3]Friedrich-Alexander-Universität Erlangen-Nürnberg, Erlangen Centre for Astroparticle Physics, Erwin-Rommel-Str. 1, 91058 Erlangen, Germany

[4]Institut d'Investigació per a la Gestió Integrada de les Zones Costaneres (IGIC) - Universitat Politècnica de València. C/ Paranimf 1 , 46730 Gandia, Spain.

[5]Aix-Marseille Université, CNRS/IN2P3, CPPM UMR 7346, 13288 Marseille, France

[6]APC, Université Paris Diderot, CNRS/IN2P3, CEA/IRFU, Observatoire de Paris, Sorbonne Paris Cité, 75205 Paris, France

[7]IFIC - Instituto de Física Corpuscular (CSIC - Universitat de València) c/ Catedrático José Beltrán, 2 E-46980 Paterna, Valencia, Spain

[8]LAM - Laboratoire d'Astrophysique de Marseille, Pôle de l'Étoile Site de Château-Gombert, rue Frédéric Joliot-Curie 38, 13388 Marseille Cedex 13, France

[9]INFN - Laboratori Nazionali del Sud (LNS), Via S. Sofia 62, 95123 Catania, Italy

[10]Nikhef, Science Park, Amsterdam, The Netherlands

[11]Huygens-Kamerlingh Onnes Laboratorium, Universiteit Leiden, The Netherlands

[12]Universiteit van Amsterdam, Instituut voor Hoge-Energie Fysica, Science Park 105, 1098 XG Amsterdam, The Netherlands

[13]INFN -Sezione di Roma, P.le Aldo Moro 2, 00185 Roma, Italy

[14]Dipartimento di Fisica dell'Università La Sapienza, P.le Aldo Moro 2, 00185 Roma, Italy

[15]Institute for Space Science, RO-077125 Bucharest, Măgurele, Romania

[16]INFN - Sezione di Bologna, Viale Berti-Pichat 6/2, 40127 Bologna, Italy

[17]INFN - Sezione di Bari, Via E. Orabona 4, 70126 Bari, Italy

[18]Géoazur, UCA, CNRS, IRD, Observatoire de la Côte d'Azur, Sophia Antipolis, France

[19]Univ. Paris-Sud , 91405 Orsay Cedex, France

[20]University Mohammed I, Laboratory of Physics of Matter and Radiations, B.P.717, Oujda 6000, Morocco

[21]Institut für Theoretische Physik und Astrophysik, Universität Würzburg, Emil-Fischer Str. 31, 97074 Würzburg, Germany

[22]Dipartimento di Fisica e Astronomia dell'Università, Viale Berti Pichat 6/2, 40127 Bologna, Italy

[23]Laboratoire de Physique Corpusculaire, Clermont Univertsité, Université Blaise Pascal, CNRS/IN2P3, BP 10448, F-63000 Clermont-Ferrand, France

[24]INFN - Sezione di Catania, Viale Andrea Doria 6, 95125 Catania, Italy

[25]LSIS, Aix Marseille Université CNRS ENSAM LSIS UMR 7296 13397 Marseille, France ; Université de Toulon CNRS LSIS UMR 7296 83957 La Garde, France ; Institut niversitaire de France, 75005 Paris, France

[26]Royal Netherlands Institute for Sea Research (NIOZ), Landsdiep 4,1797 SZ 't Horntje (Texel), The Netherlands

[27]INFN - Sezione di Genova, Via Dodecaneso 33, 16146 Genova, Italy

[28]Dipartimento di Fisica dell'Università, Via Dodecaneso 33, 16146 Genova, Italy

[29]Dr. Remeis-Sternwarte and ECAP, Universität Erlangen-Nürnberg, Sternwartstr. 7, 96049 Bamberg, Germany

[30]Moscow State University,Skobeltsyn Institute of Nuclear Physics,Leninskie gory, 119991 Moscow, Russia

[31]Mediterranean Institute of Oceanography (MIO), Aix-Marseille University, 13288, Marseille, Cedex 9, France; Université du Sud Toulon-Var, 83957, La Garde Cedex, France CNRS-INSU/IRD UM 110

[32]Dipartimento di Fisica ed Astronomia dell'Università, Viale Andrea Doria 6, 95125 Catania, Italy

[33]Direction des Sciences de la Matière - Institut de recherche sur les lois fondamentales de l'Univers - Service de Physique des Particules, CEA Saclay, 91191 Gif-sur-Yvette Cedex, France

[34]INFN - Sezione di Pisa, Largo B. Pontecorvo 3, 56127 Pisa, Italy

[35]Dipartimento di Fisica dell'Università, Largo B. Pontecorvo 3, 56127 Pisa, Italy

[36]INFN -Sezione di Napoli, Via Cintia 80126 Napoli, Italy

[37]Université de Strasbourg, IPHC, 23 rue du Loess 67037 Strasbourg, France - CNRS, UMR7178, 67037 Strasbourg, France

[38]Dipartimento di Fisica dell'Università Federico II di Napoli, Via Cintia 80126, Napoli, Italy

[39]Institut Universitaire de France, 75005 Paris, France

[40]Gran Sasso Science Institute, Viale Francesco Crispi 7, 67100 L'Aquila, Italy

E-mail: dornic@cppm.in2p3.fr, agustin.sanchez@ba.infn.it, coleiro@apc.univ-paris7.fr

Abstract. ANTARES is currently the largest neutrino telescope operating in the Northern Hemisphere, aiming at the detection of high-energy neutrinos from astrophysical sources. Neutrino telescopes constantly monitor at least one complete hemisphere of the sky, and are thus well-suited to detect neutrinos produced in transient astrophysical sources. A time-dependent search has been applied to a list of 33 x-ray binaries undergoing high flaring activities in satellite data (RXTE/ASM, MAXI and Swift/BAT) and during hardness transition states in the 2008–2012 period. The background originating from interactions of charged cosmic rays in the Earth's atmosphere is drastically reduced by requiring a directional and temporal coincidence with astrophysical phenomena. The results of this search are presented together with comparisons between the neutrino flux upper limits and the neutrino flux predictions from astrophysical models. The neutrino flux upper limits resulting from this search limit the jet parameter predictions for some astrophysical models.

Contents

1 Introduction 1

2 Selection of outburst periods 2

3 Selection of transition state periods 5

4 Time-dependent analysis 5

5 Results and discussions 6

6 Conclusion 9

1 Introduction

X-ray binaries are binary systems composed of a compact object (neutron star (NS) or stellar mass black hole (BH) candidate) orbiting a companion non-degenerate star. Due to the strong gravitational attraction, matter expelled from the companion is accreted by the compact object. Depending on the mass of the companion star and the process of matter accretion, x-ray binaries are separated into two classes: Low-Mass X-ray Binaries (LMXB) which contain an evolved companion star of spectral class later than B transferring matter to the compact object through Roche lobe overflows; and High-Mass X-ray Binaries (HMXB) consisting of a massive O or B star developing intense stellar winds, a fraction of which is accreted by the compact object. While some of these objects are seen as persistent sources, most of them exhibit occasional outbursts, making them transient sources, in particular in the radio and x-ray domains.

Recent detections of GeV–TeV gamma-ray signals from some x-ray binaries confirm that they can produce outflows containing particles accelerated away from the compact object up to relativistic speeds [1]. At the moment, it is not clear whether the high-energy particle acceleration is a common process occurring in x-ray binaries but observed only in some systems with preferred (geometrical) characteristics with respect to the line of sight, or whether it is powered by a different mechanism at work only in some specific systems.

The theoretical mechanisms of gamma-ray production from x-ray binaries generally assume (very-) high-energy photon emission from the interaction of a relativistic outflow from the compact object with the wind and radiation emitted by the companion star. The outflow can take different shapes. In microquasars [2] the high-energy emission is due to accretion energy released in the form of a collimated relativistic jet, detected in the radio domain through synchrotron emission. On the contrary, in other binary systems, high-energy emission can occur in a wide-angle shocked region, at the interface between pulsar and stellar winds [3].

Even if a rich variety of binary systems seem to be cosmic accelerators, some major issues are still open: are jets a common feature of x-ray binary systems? What is the particle acceleration mechanism at work in these systems? Is it unique? Constraining the jet composition and its baryonic content will help answering these questions. Indeed, the jet composition should be affected by the outflow-launching processes. For instance, jets powered by an accretion disk are likely to contain baryons [4] while jets which get their power from black

hole spin are expected to be purely leptonic [5]. Up to now, a hadronic component has been identified in only two x-ray binaries (SS 433 and 4U 1630-472) [5, 6] while a population of cold baryons present in the relativistic jet of Cyg X-1 has been proposed [7].

When baryons are present in an x-ray binary outflow, high-energy neutrinos might be produced either from p-gamma interaction in the jets [8] or from pp interactions between high-energy protons ejected by the compact object with matter expelled from the companion star [9, 10]. The detection of high-energy neutrinos from an x-ray binary system would definitively confirm the presence of relativistic protons in the outflow, and thus further constrain the particle acceleration mechanism.

The ANTARES Collaboration completed the construction of a neutrino telescope in the Mediterranean Sea with the connection of its twelfth detector line in May 2008 [11]. The telescope is located 20 km off the Southern coast of France (42°48'N, 6°10'E), at a depth of 2475 m. In the ANTARES telescope, events are primarily detected by observing the Cherenkov light induced by relativistic muons in the darkness of the deep sea. Owing to their low interaction probablility, only neutrinos have the ability to cross the Earth. Therefore, an upgoing muon is an unambiguous signature of a neutrino interaction close to the detector. To distinguish astrophysical neutrino events from background events (muons and neutrinos) generated in the atmosphere, energy and direction reconstructions have been used in several searches [12, 13]. To improve the signal-to-noise discrimination, the arrival time information can be used to significantly reduce the effective background [14].

In this paper, the results of a time-dependent search for cosmic neutrino sources using the ANTARES data taken from 2008 to 2012 is presented. This extends a previous ANTARES analysis [15] where only six sources and the first three years of data-taking were considered. It is also complementary to a previous IceCube transient analysis [16] which considered few x-ray binary systems. However, the ANTARES location in the northern hemisphere, and its lower neutrino energy threshold in comparison with IceCube, make it well-suited to study neutrino emission from such galactic sources. Neutrino emission has been searched-for during outburst periods of x-ray binaries characterised by the variability of their soft and hard x-ray flux density [17]. Jet emission, probably linked to particle acceleration and thus potential neutrino emission, usually occurs during periods of high levels of hard x-ray flux density (called hard states) and during transition periods (intermediate states) between a hard state and a soft state. Sections 2 and 3 present the selection of outburst periods selection from x-ray light curves, during hard and intermediate states respectively. Section 4 details the statistical approach used to perform the analysis, while results are provided and discussed in Section 5. Conclusions are drawn in Section 6.

2 Selection of outburst periods

The time-dependent analysis described in the following section is applied to a list of x-ray binaries exhibiting outburst periods in their light curves. The light curves are obtained mainly using the Swift/BAT telescope[1]. These data are complemented by those from other instruments: RXTE/ASM[2] and MAXI[3]. A maximum likelihood block (MLB) algorithm [18] is used to remove noise from the light curve by iterating over the data points and selecting periods during which data are consistent with a constant flux within statistical errors. This algorithm is applied independently to all the light curves from all the satellites. Depending on the time period and the availability of the different instruments, outbursts are better observed in one apparatus compared to others. As the energy range and the sensitivity of

these telescopes are different, it is not easy to combine measurements into a single time-dependent function to describe the light curve. The value of the steady state (i.e. baseline, BL) and its fluctuation (σ_{BL}) are determined with a Gaussian fit of the lower part of the distribution of the flux. The baseline is subtracted from the light curve and the amplitude is converted to a relative amplitude by dividing by σ_{BL}. Finally, the relative light curves from different instruments are merged, as can be seen for the sample source 4U 1705-440 in Figure 1. This is used to produce the time probability functions for the analysis (see Section 4).

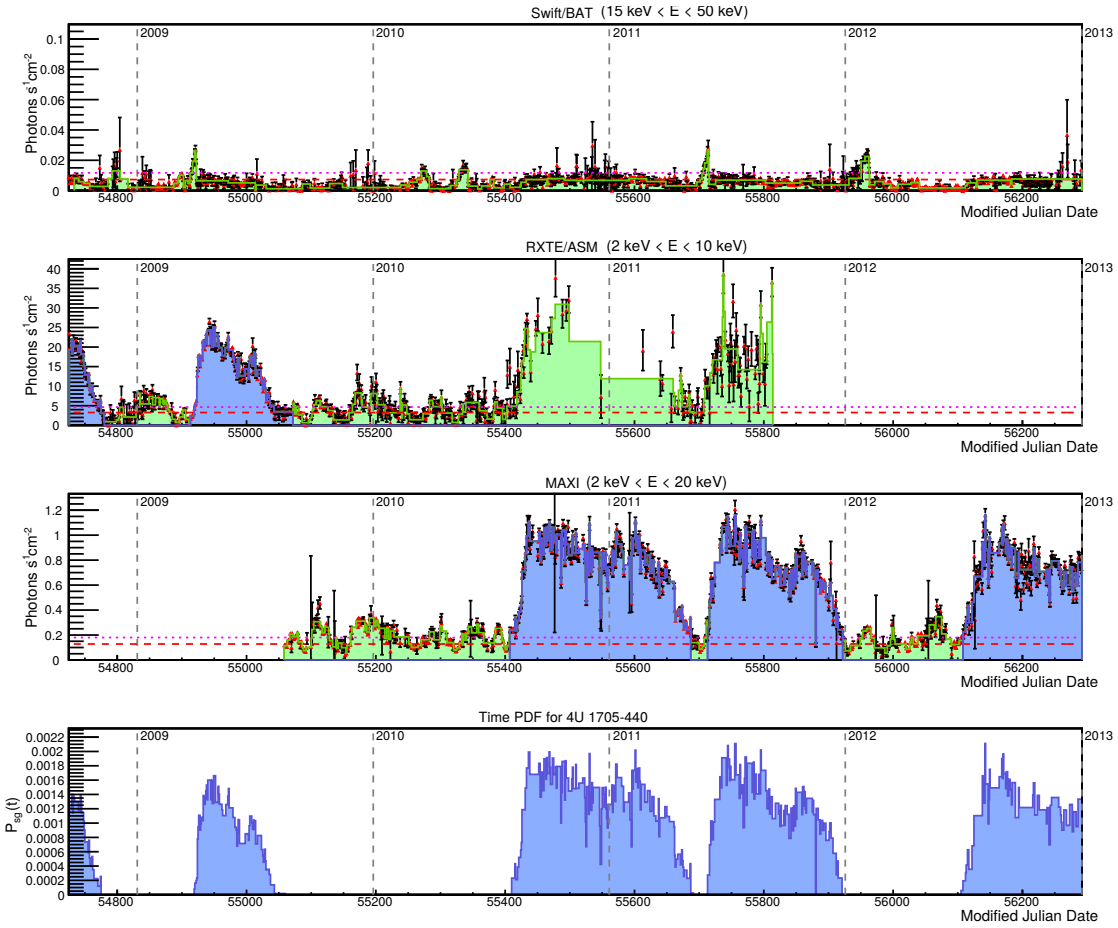

Figure 1. Light curves for 4U 1705-440 as seen by Swift/BAT, RXTE/ASM and MAXI during the studied period. The estimated baseline emissions, BL, (red lines) and $BL+1\sigma_{BL}$ (magenta lines) are also shown. Histograms correspond to the light curves treated with the MLB algorithm. The blue histograms represent the selected flaring periods of each light curve, merged to produce the time PDF (bottom). Green histograms show periods of each light curve not selected for this analysis.

The flaring periods are defined from the blocks of the light curve characterised by the MLB algorithm in three main steps. Firstly, seeds are identified by searching for blocks with an amplitude above $BL + 8\sigma_{BL}$. Then, each period is extended forward and backward up

[1]http://swift.gsfc.nasa.gov/results/transients
[2]http://xte.mit.edu/ASM_lc.html
[3]http://maxi.riken.jp

to an emission compatible with $BL + 1\sigma_{BL}$. A delay of 0.5 days is added before and after the flare in order to take into account that the precise time of the flare is not known (one-day binned light curve). Finally, spurious flares are discarded if they are not visible by at least one other instrument. The final list includes 33 x-ray binaries: 1 HMXB (BH), 11 HMXB (NS), 8 HMXB (BH candidate), 10 LMXB (NS) and 3 XRB (BH candidate), as reported in Table 1.

Table 1. List of 33 x-ray binaries with significant flares selected for this analysis.

Name	Class	RA [°]	Dec [°]
Cyg X-1	HMXB (BH)	230.170	-57.167
1A 0535+262	HMXB (NS)	84.727	26.316
1A 1118-61	HMXB (NS)	170.238	-61.917
Ginga 1843+00	HMXB (NS)	281.404	0.863
GS 0834-430	HMXB (NS)	128.979	-43.185
GX 304-1	HMXB (NS)	195.321	-61.602
H 1417-624	HMXB (NS)	215.303	-62.698
MXB 0656-072	HMXB (NS)	104.572	-7.210
XTE J1946+274	HMXB (NS)	296.414	27.365
GX 1+4	HMXB (NS)	263.009	-24.746
MAXI J1409-619	HMXB (NS)	212.011	-61.984
GRO J1008-57	HMXB (NS)	152.433	-58.295
GX 339-4	LMXB (BHC)	255.706	-48.784
4U 1630-472	LMXB (BHC)	248.504	-47.393
IGR J17091-3624	LMXB (BHC)	257.282	-36.407
IGR J17464-3213	LMXB (BHC)	266.565	-32.234
MAXI J1659-152	LMXB (BHC)	254.757	-15.258
SWIFT J1910.2-0546	LMXB (BHC)	287.595	-5.799
XTE J1752-223	LMXB (BHC)	268.063	-22.342
SWIFT J1539.2-6227	LMXB (BHC)	234.800	-62.467
4U 1954+31	LMXB (NS)	298.926	32.097
Aql X-1	LMXB (NS)	287.817	0.585
Cir X-1	LMXB (NS)	230.170	-57.167
EX O1745-248	LMXB (NS)	267.022	-24.780
H 1608-522	LMXB (NS)	243.179	-52.423
SAX J1808.4-3658	LMXB (NS)	272.115	-36.977
XTE J1810-189	LMXB (NS)	272.586	-19.070
4U 1636-536	LMXB (NS)	250.231	-53.751
4U 1705-440	LMXB (NS)	257.225	-44.102
IGR J17473-2721	LMXB (NS)	266.825	-27.344
MAXI J1836-194	XRB (BHC)	278.931	-19.320
XTE J1652-453	XRB (BHC)	253.085	-45.344
SWIFT J1842.5-1124	XRB (BHC)	280.573	-11.418

3 Selection of transition state periods

Spectral transition states of XRB are difficult to define: there are no regular observations with x-ray satellites, and statistics are very low due to the inaccurate measurement of the hardness ratio, defined as the ratio of counts in different x-ray wavebands. Considering the difficulties of an extensive coverage of the transition states of XRB, the selection of the these transition periods relies on the alerts reported in *Astronomer's Telegram* [4]. The selected 19 alerts in the period 2008–2012, distributed among 8 sources, and the corresponding transition periods, are shown in Table 2. Considering the lack of information on the time variation of flux, a constant emission during each of the reported dates has been assumed.

Table 2. List of 8 x-ray binaries with hardness transition states reported in *Astronomer's Telegram*.

Name	#ATel	Transition State Periods [MJD] (days)
GX 339-4	#2577 #2593 #3117 #3191	55303 – 55305 (2) 55308 – 55309 (1) 55315 – 55316 (1) 55318 – 55319 (1) 55580 – 55581 (1) 55616 – 55617 (1)
H 1608-522	#2072 #2467	54960 – 54976 (16)
IGR J17091-3624	#3179 #3196	55611 – 55612 (1) 55962 – 55964 (2)
IGR J17464-3213	#1804 #1813 #3301 #3842	54752 – 54759 (7) 55671 – 55672 (1) 55925 – 55927 (2)
MAXI J1659-152	#2951 #2999	55481 – 55487 (6) 55500 – 55502 (2)
SWIFT J1910.2-0546	#4139 #4273	56094 – 56095 (1) 56131 – 56133 (2)
XTE J1652-453	#2219	55010 – 55085 (75)
XTE J1752-223	#2391 #2518	55219 – 55220 (1) 55492 – 55493 (1)

4 Time-dependent analysis

The ANTARES data collected between 2008 and 2012, corresponding to 1044 days of livetime, are analysed to search for neutrino events around the selected sources, in coincidence with the time periods defined in the previous sections. The statistical method adopted to infer the presence of a signal on top of the atmospheric neutrino background, or alternatively set upper limits on the neutrino flux is an unbinned method based on an extended maximum likelihood ratio test statistic. It has been previously used to search for neutrinos from gamma-ray flaring blazars [19]. The likelihood, $\mathcal{L}$, is defined as:

$$\ln \mathcal{L}(\mathcal{N}_S) = \left(\sum_{i=1}^{N} \ln[\mathcal{N}_S \mathcal{S}_i + \mathcal{N}_B \mathcal{B}_i] \right) - [\mathcal{N}_S + \mathcal{N}_B] \tag{4.1}$$

where $\mathcal{S}_i$ and $\mathcal{B}_i$ are the probabilities for signal and background for an event i, respectively, and $\mathcal{N}_S$ (not known) and $\mathcal{N}_B$ (known) are the number of expected signal and background events in the data sample. N is the total number of events in the considered data sample. To discriminate the signal-like events from background, these probabilities are described by the product of three components related to the direction, energy, and timing of each event. For an event i, the signal probability is:

$$\mathcal{S}_i = \mathcal{S}^{\text{space}}(\Psi_i) \cdot \mathcal{S}^{\text{energy}}(dE/dX_i) \cdot \mathcal{S}^{\text{time}}(t_i + t_{\text{lag}}) \tag{4.2}$$

[4] *http://www.astronomerstelegram.org*

Here, $\mathcal{S}^{\text{space}}$ is a parametrisation of the point spread function, i.e., $\mathcal{S}^{\text{space}}(\Psi_i)$ is the probability to reconstruct an event i at an angular distance Ψ_i from the true source location. The energy PDF, $\mathcal{S}^{\text{energy}}$, is the normalised distribution of the muon energy estimator, dE/dX, of an event according to the studied energy spectrum. To cover the majority of the range allowed by the models [8, 20] accessible to the ANTARES sensitivity, three neutrino-energy differential spectra are tested in this analysis: E^{-2}, $E^{-2}\exp(-E/100\text{ TeV})$ and $E^{-2}\exp(-E/10\text{ TeV})$, where E is the neutrino energy. The shape of the time PDF, $\mathcal{S}^{\text{time}}$, for the signal event is extracted directly from the gamma-ray light curve parametrisation, as described in the previous sections, assuming proportionality between gamma-ray and neutrino fluxes. A possible lag of up to ± 5 days has been introduced in the likelihood to allow for small lags in the proportionality. This corresponds to a possible shift of the entire time PDF. The lag parameter is fitted in the likelihood maximisation together with the number of fitted signal events in the data. The background probability for an event i is:

$$\mathcal{B}_i = \mathcal{B}^{\text{space}}(\delta_i) \cdot \mathcal{B}^{\text{energy}}(dE/dX_i) \cdot \mathcal{B}^{\text{time}}(t_i) \tag{4.3}$$

where the directional PDF, $\mathcal{B}^{\text{space}}$, the energy PDF, $\mathcal{B}^{\text{energy}}$, and the time PDF, $\mathcal{B}^{\text{time}}$, for the background are derived from data using, respectively, the observed declination, δ_i, distribution of selected events in the sample, the measured distribution of the energy estimator, and the observed time distribution of all the reconstructed muons.

The goal of the unbinned search is to determine, in a given direction in the sky and at a given time, the relative contribution of each component, and to calculate the probability to have a signal above a given background model. This is done via the test statistic, λ, defined as the ratio of the probability for the hypothesis of background plus signal over the probability of only background:

$$\lambda = \sum_{i=1}^{N} \ln \frac{\mathcal{L}(\mathcal{N}_{\text{S}})}{\mathcal{L}(\mathcal{N}_{\text{S}} = 0)} \tag{4.4}$$

The evaluation of the test statistic is performed by generating pseudo-experiments simulating background and signal in a 30° cone around the considered source according to the background-only and background plus signal hypotheses. The performance of the time-dependent analysis is computed using toy experiments. For time ranges characteristic of flaring activity, the time-dependent search presented here improves the discovery potential by on-average a factor 2-3 with respect to a standard time-integrated point-source search [12], under the assumption that the neutrino emission is correlated with the x-ray flaring activity.

5 Results and discussions

Only one source exhibited a significant signal excess during an x-ray flare: GX 1+4, with 287 days of flare duration included in the analysis, shows a p-value of 4.1% with a fitted signal of 0.7 events and a lag of -4 days, which is obtained with the 100 TeV cutoff energy spectrum. This result is due to one (three) events in a cone of 1 (3) degrees in coincidence with x-ray outbursts detected by RXTE/ASM and Swift/BAT. Figure 2 shows the light curve of GX 1+4 with the time of the neutrino candidates, the estimated energy distribution, and the angular distribution of the events around the position of this source. The post-trial probability, computed by taking into account the 33 searches, is 72%, and is thus compatible with background fluctuations. In the hardness transition state analysis, no significant excess has been found, with a 77% post-trial probability for the full analysis.

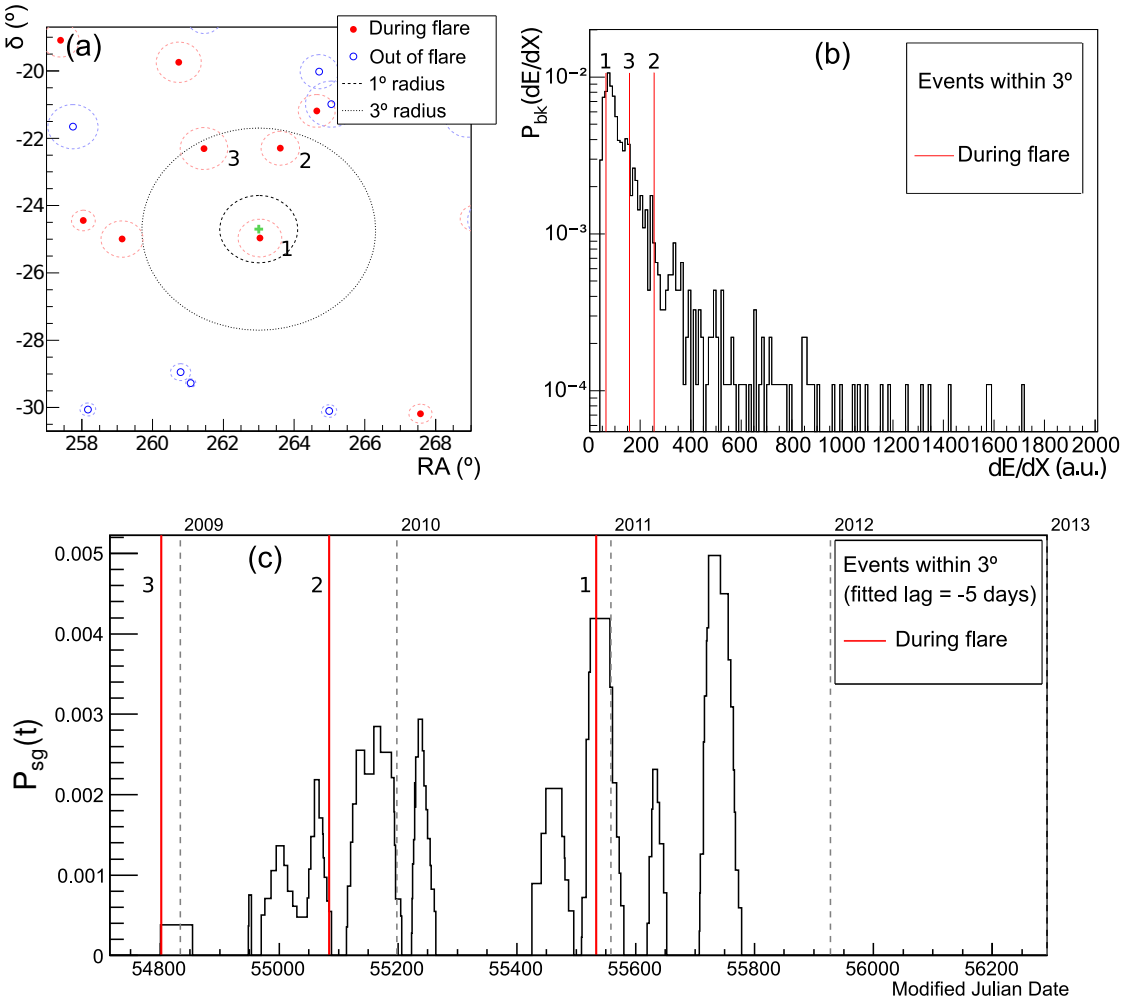

Figure 2. Results of this analysis for GX 1+4. (a) Event map around the direction of GX 1+4 indicated by the green cross. The full red (hollow blue) dots indicate the events (not) in time coincidence with the selected flares. The size of the circle around the dots is proportional to the estimated angular uncertainty for each event. The three closest events from the source direction are labeled 1, 2 and 3. (b) Distribution of the estimated energy dE/dX in a $\pm 10^\circ$ declination band around the source direction. The red line displays the values of the three most significant events. (c) Time distribution of $\mathcal{B}^{\text{time}}$. The red line displays the times of the 3 ANTARES events indicated in panel (a).

In the absence of a discovery, upper limits on the neutrino fluence, $\mathcal{F}_\nu$, the energy flux, F, and the differential flux normalisation, ϕ_0, at 90% confidence level are computed using 5-95% of the energy range as:

$$\mathcal{F}_\nu = \Delta t \cdot F = \Delta t \int_{E_{\min}}^{E_{\max}} \mathrm{d}E \cdot E \cdot \phi_0 \cdot \mathcal{S}(E) = \Delta t \cdot \phi_0 \cdot \mathrm{I}(E) \tag{5.1}$$

where $\mathcal{S}(E)$ is the dimensionless neutrino spectrum, e.g. for the E^{-2} spectrum, $\mathrm{d}N/\mathrm{d}E = \phi_0 \cdot \mathcal{S}(E) = \phi_0 \cdot (E/\mathrm{GeV})^{-2}$. The limits are calculated according to the classical (frequentist) method for upper limits [21] and are summarised in Table 3. Figure 3 displays these upper limits. Systematic uncertainties of 15% on the angular resolution and 15% on the detector

acceptance have been included in the upper limit calculations [12].

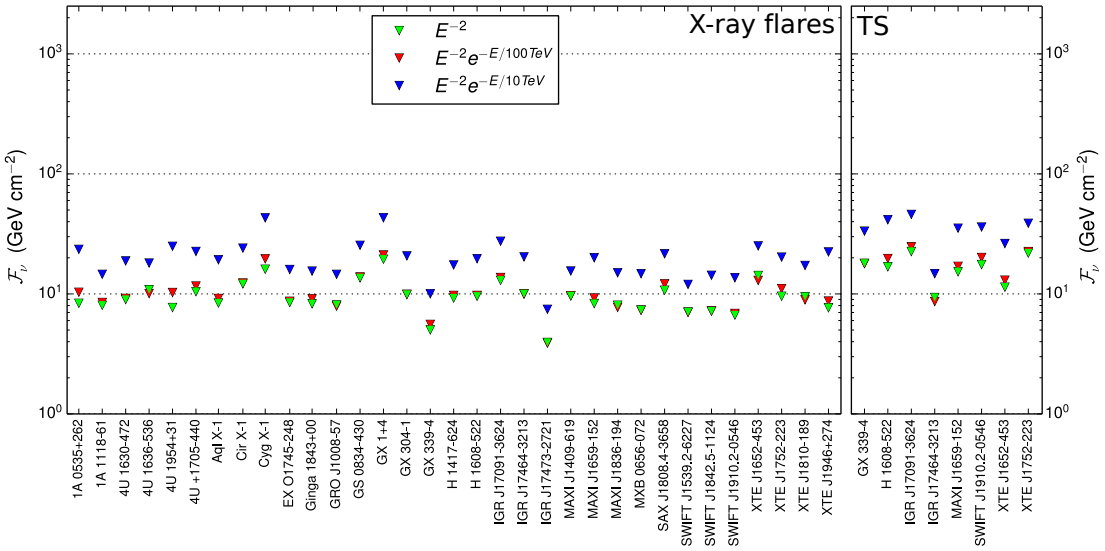

Figure 3. Upper limits at 90% C.L. on the neutrino fluence for the 33 XRB with outburst periods (left) and for the 8 XRB with transition state periods (right) in the case of E^{-2} (green triangles), $E^{-2}\exp(-E/100$ TeV) (red triangles) and $E^{-2}\exp(-E/10$ TeV) (blue triangles) neutrino energy spectra.

The neutrino energy flux predictions, $F_{\rm pred}$, for seven microquasars have been computed according to the photohadronic model [8]. Since they are less stringent, the energy flux upper limits of the transition states are not discussed hereafter. Thus, in the following, only the neutrino energy flux upper limits related to the hard state periods are considered. Using the latest measurements of their distance and of the jet parameters, the model predicts the neutrino energy flux based on the radio luminosity of the jets observed in radio during flares. The derived neutrino energy flux depends on the fraction of jet kinetic energy, $L_{\rm jet}$, converted respectively to relativistic electrons and magnetic field, $\eta_{\rm e}$, and protons $\eta_{\rm p}$, and the fraction of proton energy converted into pions, f_π, which depends in turn on the energy to which protons are accelerated. Resolved and unresolved sources are considered separately. In the following, resolved sources refer to microquasar jets resolved by radio interferometry which enables the physical parameters of the jet to be prebed (Table 4).

For resolved sources, the neutrino energy flux is estimated from the radio flux density, S_f, at frequency f, the distance of the source, d, the size of the emitting region, l, the jet Lorentz factor, Γ, the jet velocity, β, the angle, θ, between the line of sight and the jet, and the jet opening angle, ψ. The ratio of the minimum and maximum electron Lorentz factors, respectively $\gamma_{\rm min}$ and $\gamma_{\rm max}$, is assumed to be equal to 100, while ψ is taken equal to a conservative value of 20° except in the case of Cyg X-1 [22]. All the other parameters have been retrieved from the literature and are listed in Table 4 along with their uncertainties and

references. When θ is not observationally constrained, all the values between 0 and 90° are considered. Similarly, if the bulk Lorentz factor, Γ, of the jet is poorly known, all the potential values are tested. These uncertainties, together with the error on the other jet parameters, are taken into account to derive the range of neutrino energy fluxes $F_{\rm pred}$ satisfying the model which is linearly dependent on $\eta_{\rm e}/\eta_{\rm p}$.

The resulting predictions are compared with the upper limits obtained with ANTARES data under the hypothesis of a cutoff at 100 TeV in the neutrino flux, to account for limits in the acceleration process included in the model [8]. As an example, Fig. 4 shows how the predicted flux compares with this result as a function of the jet parameter β for resolved microquasars Cyg X-1, Cir X-1 and MAXI J1659-152 [5]. Comparing the predicted flux and the ANTARES neutrino energy flux upper limits, upper limits at 90% C.L. on $\eta_{\rm p}/\eta_{\rm e}$ are set. These limits have been derived taking into account the discrepancy between Lorentz factors reported in radio observations, and uncertainties on the opening angle of the jet, the distance of the source, and on the inclination angle between the line of sight and the jet. Results are given for Cyg X-1, Cir X-1 and MAXI J1659-152 in Fig. 4 and in Table 4.

However, the potential variability of the Lorentz factor during a burst and between the periods of activity of the source are not taken into account in this calculation. Thus, constraints on baryon loading may have different implications: the proton component in the jet can be negligible in comparison with the electromagnetic component, the proton energy fraction converted to pions can be less significant than the values considered [8], and/or the jet Lorentz factor is lower than the constraints set by radio observations.

For unresolved sources, the jet kinetic power is evaluated from the jet synchrotron luminosity derived from the flux density, $S_{f_{\rm break}}$, at the frequency break, $f_{\rm break}$, between optically thick and optically thin radio emission, and the spectral index, α_R [8]. These values are reported in Table 5. When no spectral index value is provided in the literature, $\alpha_R = 0$ is assumed as given by the standard jet radio emission theory [24]. Again, the neutrino energy flux is linearly dependent on f_π and $\eta_{\rm e}/\eta_{\rm p}$. The predicted neutrino energy flux $\eta_{\rm e}/\eta_{\rm p} F_{\rm pred}$ and the upper limits on $\eta_{\rm p}/\eta_{\rm e}$ are given in Table 5. The results for both resolved and unresolved sources are summarised in Figure 5.

In [25], the authors have provided a calculation of the high-energy neutrino emission from GX 339-4 in the hypothesis that the primary spectrum of the injected particles in the jets has spectral indexes $-1.8 > \alpha > -2.0$ and that the ratio between proton and electron energy is equal to 1 and 100 (Figure 6). The model with a ratio $\eta_{\rm p}/\eta_{\rm e}$ equal to 100 is excluded by the present limit.

6 Conclusion

This paper discusses the time-dependent search for neutrinos from x-ray binaries using the data taken with the full ANTARES detector between 2008 and 2012. This search has been applied to a list of 33 XRB sources, 8 of them during hardness transition periods. The search did not result in a statistically significant excess above the expected background from atmospheric neutrino and muon events. The most significant correlation during x-ray flares is found

[5] The energy flux upper limit obtained for H 1743-322 is around 2 orders of magnitude higher than the expectations [8]. Thus, this source is not included in Fig. 4.

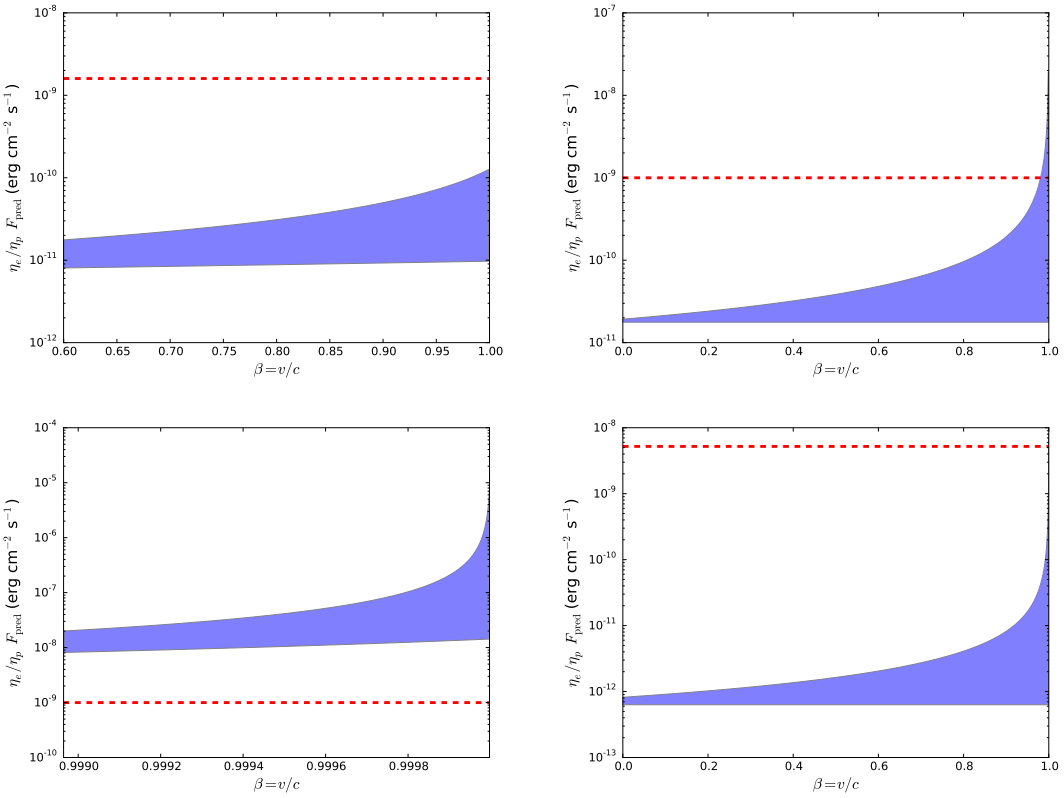

Figure 4. Comparison of the energy flux upper limit at 90% C.L. provided by ANTARES (red dashed line) with the predictions [8] as a function of the jet velocity, β: Cyg X-1 (top left), Cir X-1 with jet parameters [28] (top right), Cir X-1 with jet parameters [23] (bottom left) and MAXI J1659-152 (bottom right).

for the source GX 1+4, for which 3 neutrino candidate events were detected in time/spatial coincidence with x-ray emission. However, the post-trial probability is 72%, thus compatible with background fluctuations. A comparison with predictions from several models shows that for some sources, the upper limits start to constrain the parameter space of the expectations from hadronic jet emission models. Therefore, with additional data from ANTARES and with the order of magnitude sensitivity improvement expected from the next generation neutrino telescope, KM3NeT [26], the prospects for future searches for neutrino emission from x-ray binaries are very promising.

Acknowledgments

The authors acknowledge the financial support of the funding agencies: Centre National de la Recherche Scientifique (CNRS), Commissariat à l'énergie atomique et aux énergies alternatives (CEA), Commission Européenne (FEDER fund and Marie Curie Program), Institut Universitaire de France (IUF), IdEx program and UnivEarthS Labex program at Sorbonne Paris Cité (ANR-10-LABX-0023 and ANR-11-IDEX-0005-02), Labex OCEVU (ANR-11-LABX-0060) and the A*MIDEX project (ANR-11-IDEX-0001-02), Région Île-de-France (DIM-ACAV), Région Alsace (contrat CPER), Région Provence-Alpes-Côte d'Azur, Dépar-

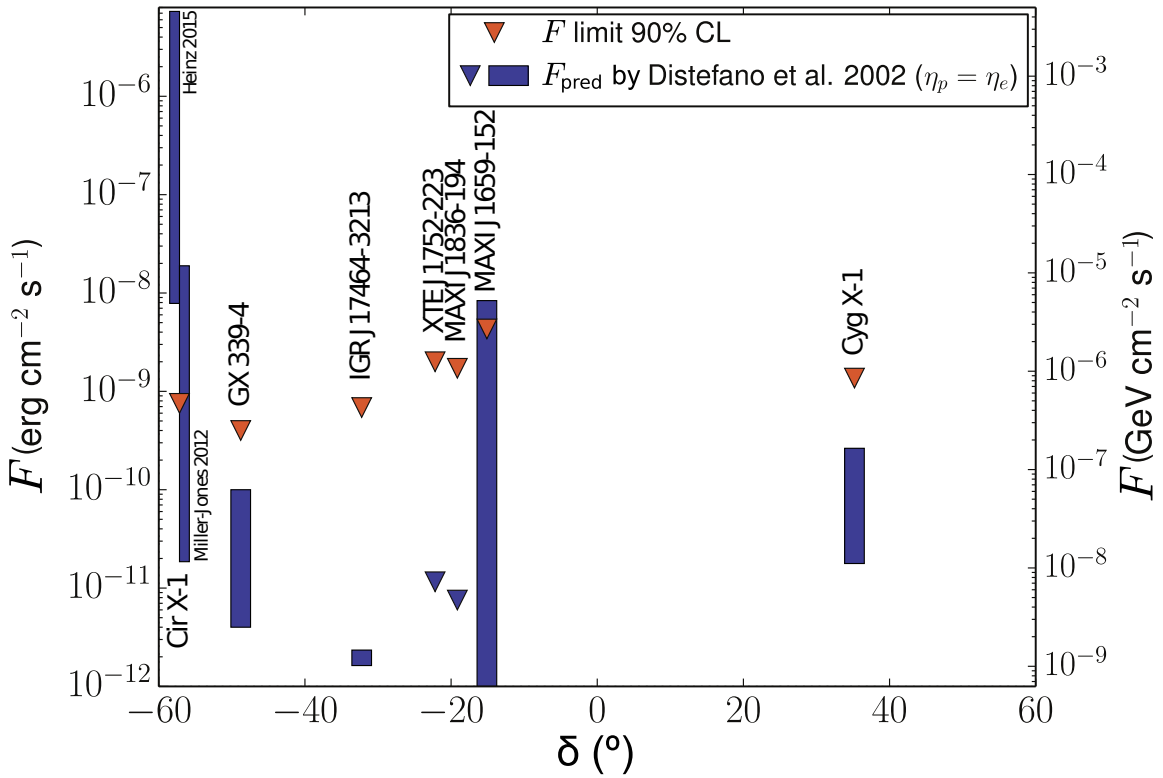

Figure 5. Upper limits at 90% C.L. on the neutrino energy flux obtained in this analysis considering a $E^{-2}\exp(-\sqrt{(E/100\text{ TeV})})$ spectra, compared with the expectations [8] assuming energy equipartition between electrons and protons. The blue rectangles show the expectations from [8] taking into account the uncertainty on the jet velocity. For the unresolved microquasars XTE J1752-223 and MAXI J1836-194, a single energy flux prediction value is given, since no detail on the jet velocity is available in the literature.

tement du Var and Ville de La Seyne-sur-Mer, France; Bundesministerium für Bildung und Forschung (BMBF), Germany; Istituto Nazionale di Fisica Nucleare (INFN), Italy; Stichting voor Fundamenteel Onderzoek der Materie (FOM), Nederlandse organisatie voor Wetenschappelijk Onderzoek (NWO), the Netherlands; Council of the President of the Russian Federation for young scientists and leading scientific schools supporting grants, Russia; National Authority for Scientific Research (ANCS), Romania; Ministerio de Economía y Competitividad (MINECO): Plan Estatal de Investigación (refs. FPA2015-65150-C3-1-P, -2-P and -3-P, (MINECO/FEDER)), Severo Ochoa Centre of Excellence and MultiDark Consolider (MINECO), and Prometeo and Grisolía programs (Generalitat Valenciana), Spain; Agence de l'Oriental and CNRST, Morocco. We also acknowledge the technical support of Ifremer, AIM and Foselev Marine for the sea operation and the CC-IN2P3 for the computing facilities.

References

[1] M. Tavani *et al.*, 2009, Nature, 462, 620.

[2] I.F. Mirabel & L.F. Rodríguez, 1994, Nature, 371, 46.

[3] G. Dubus, 2013, A&ARv, 21, 64.

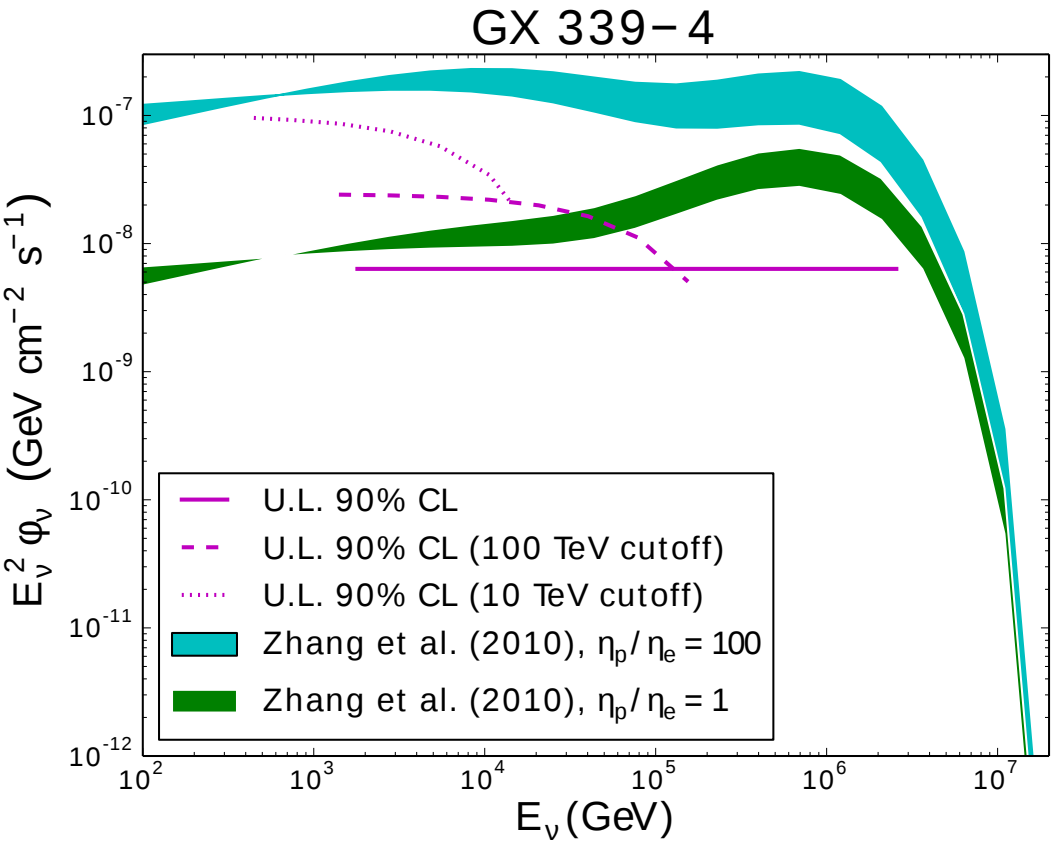
GX 339−4
$E_\nu^2 \Phi_\nu$ (GeV cm^{-2} s^{-1})
E_ν (GeV)
U.L. 90% CL
U.L. 90% CL (100 TeV cutoff)
U.L. 90% CL (10 TeV cutoff)
Zhang et al. (2010), $\eta_p/\eta_e = 100$
Zhang et al. (2010), $\eta_p/\eta_e = 1$

Figure 6. Upper limits at 90% C.L. on the neutrino flux for GX 339-4, with the energy spectrum described in Section 4, compared to the predictions [25] for spectral indexes of the injected particles $-1.8 > \alpha > -2.0$ and the ratio $n_{\rm p}/n_{\rm e}$ equal to 1 and 100.

[4] R.D. Blandford & D.G. Payne, 1982, MNRAS, 199, 883.

[5] M.D. Trigo, J.C.A. Miller-Jones, S. Migliari, J.W. Broderick, T. Tzioumis, 2013, Nature, 504, 260.

[6] S. Migliari, R. Fender, M. Mendez, 2002, Science, 297, 1673.

[7] S. Heinz, 2006, ApJ, 636, 316.

[8] C. Distefano, D. Guetta, E. Waxman, A. Levinson, 2002, ApJ, 575, 378.

[9] A. Neronov & M. Ribordy, 2009, Phys. Rev. D, 79, 043013.

[10] N. Sahakyan, G. Piano, M. Tavani, 2014, ApJ, 745, L7.

[11] M. Ageron *et al.*, Nucl. Instrum. Meth. A 656 (2011) 11-38.

[12] S. Adrián-Martínez *et al.*, ApJ, 2012, 760, 53.

[13] J.A. Aguilar *et al.*, Phys. Lett. B 696, 2011, 16-22.

[14] S. Adrián-Martínez *et al.*, *A&A* 559, A9 (2013).

[15] S. Adrián-Martínez *et al.* Journal of High Energy Astrophysics 3-4(2014) 9-17.

[16] M.G. Aartsen *et al.*, 2015, ApJ, 807, 46.

[17] R.A. Remillard & J.E. McClintock, 2006, ARA&A, 44, 49.

[18] J.D. Scargle, The Astrophysical Journal Supplement Series, 45, 1-71, 1981; J.D. Scargle, Astrophys. J., 504, 1998, 405-418; J.D. Scargle *et al.*, Astrophys.J. 764 (2013) 167.

[19] S. Adrián-Martínez *et al.*, JCAP12 (2015) 014.

[20] A. Kappes, J. Hinton, C. Stegmann, F.A. Aharonian, Astrophys. J. 656(2007) 870-896.

[21] J. Neyman, 1937, Phil. Trans. Royal Soc. London, Series A, 236, 333.

[22] J.C.A. Miller-Jones, R.P. Fender, & E. Nakar, 2006, MNRAS, 367, 1432.

[23] S. Heinz *et al.*, 2015, ApJ, 806, 265.

[24] R.D. Blandford & A. Königl, 1979, ApJ, 232, 34.

[25] J.F. Zhang, Y.G. Feng, M.C. Lei, Y.Y. Tang, Y.P. Tian, 2010, MNRAS, 407, 2468.

[26] S. Adrián-Martínez *et al.*, J. Phys. G: Nucl. Part. Phys. 43 (2016) 084001.

[27] A.M. Stirling, R.E. Spencer, C.J. de la Force, M.A. Garrett, R.P. Fender, R.N. Ogley, 2001, MNRAS, 327, 1273.

[28] J.C.A. Miller-Jones *et al.*, 2012, MNRAS, 419, 49.

[29] S. Corbel, P. Kaaret, R.P. Fender, A.K. Tzioumis, J.A. Tomsick, J.A. Orosz, 2005, ApJ, 632, 504.

[30] Z. Paragi, A.J. van der Horst, T. Belloni, J.C.A. Miller-Jones, J. Linford, G. Taylor, J. Yang, M.A. Garrett, J. Granot, C. Kouveliotou, E. Kuulkers, R.A.M.J. Wijers , 2013, MNRAS, 432, 1319.

[31] J.F. Steiner, J.E. McClintock, M.J. Reid, 2012, ApJ, 745, 7.

[32] D.M. Russell *et al.*, 2013, MNRAS, 429, 815.

Table 3. Table of upper limits at 90% C.L. during x-ray flares and hardness transition states (TS) analyses. For each source is shown the livetime, LT, and for each spectra the energy integral, I(E), the differential flux normalisation, ϕ_0, the mean energy flux, F and the fluence, $\mathcal{F}_\nu$.

Source	LT	E^{-2}				$E^{-2} \cdot \exp(-E/100\,\mathrm{TeV}$				$E^{-2} \cdot \exp(-E/10\,\mathrm{TeV})$			
		I(E)	ϕ_0	F	$\mathcal{F}_\nu$	I(E)	ϕ_0	F	$\mathcal{F}_\nu$	I(E)	ϕ_0	F	$\mathcal{F}_\nu$
1A 0535+262	66	7.0	2.1	1.5	8.4	3.4	5.4	1.8	10	2.3	1.8	4.1	24
1A 1118-61	55	6.7	2.5	1.7	8.1	3.8	4.7	1.8	8.5	2.6	1.2	3.1	15
4U 1630-472	144	7.1	1.0	0.7	9.0	3.9	1.9	0.74	9.2	2.5	0.60	1.5	19
4U 1636-536	43	7.0	4.2	2.9	11	3.9	7.1	2.7	10	2.6	1.9	4.9	18
4U 1954+31	32	7.2	3.9	2.8	7.7	3.3	12	3.8	10	2.2	4.1	9.1	25
4U +1705-440	634	7.0	0.27	0.2	10	3.7	0.57	0.21	12	2.5	0.16	0.41	23
Aql X-1	131	7.0	1.1	0.7	8.4	3.7	2.2	0.81	9.2	2.5	0.69	1.7	19
Cir X-1	232	6.8	0.89	0.6	12	3.8	1.6	0.62	12	2.5	0.48	1.2	24
Cyg X-1	228	7.0	1.2	0.8	16	3.2	3.1	1.0	20	2.2	0.99	2.2	43
EX O1745-248	55	7.1	2.5	1.8	8.5	3.8	4.8	1.8	8.7	2.5	1.3	3.4	16
Ginga 1843+00	5	6.9	28	19	8.3	3.6	58	21	9.1	2.5	14	36	16
GRO J1008-57	146	6.8	0.95	0.6	8.1	3.9	1.6	0.63	7.9	2.6	0.45	1.2	15
GS 0834-430	74	7.2	3.0	2.1	14	3.9	5.7	2.2	14	2.6	1.6	4.0	25
GX 1+4	287	7.1	1.1	0.8	19	3.8	2.3	0.85	21	2.5	0.70	1.7	43
GX 304-1	200	6.7	0.86	0.6	10	3.9	1.5	0.58	9.9	2.5	0.48	1.2	21
GX 339-4	184	7.1	0.45	0.3	5.0	3.8	0.93	0.35	5.6	2.5	0.25	0.63	10
H 1417-624	64	6.6	2.6	1.7	9.3	3.8	4.7	1.8	9.7	2.5	1.3	3.2	17
H 1608-522	487	7.0	0.33	0.2	10	3.8	0.60	0.23	9.7	2.5	0.19	0.47	20
IGR J17091-3624	34	7.2	6.1	4.4	13	3.8	12	4.7	14	2.5	3.7	9.3	28
IGR J17464-3213	231	7.1	0.70	0.5	10	3.8	1.3	0.50	10	2.5	0.41	1.0	20
IGR J17473-2721	6	7.2	11	8.2	3.9	3.8	21	8.1	3.9	2.5	6.2	15	7.5

MAXI J1409-619	24	6.7	7.1	4.7	10	3.9	12	4.8	9.7	2.6	3.0	7.7	16
MAXI J1659-152	31	7.0	4.4	3.1	8.3	3.7	9.3	3.5	9.3	2.5	3.0	7.5	20
MAXI J1836-194	76	7.0	1.7	1.2	8.1	3.8	3.1	1.2	7.7	2.5	0.92	2.3	15
MXB 0656-072	18	6.9	6.8	4.7	7.4	3.7	13	4.7	7.3	2.5	3.9	9.5	15
SAX J1808.4-3658	28	7.2	6.1	4.4	11	3.8	13	5.0	12	2.5	3.5	8.9	22
SWIFT J1539.2-6227	23	6.6	5.4	3.6	7.1	3.9	9.2	3.6	7.0	2.6	2.4	6.1	12
SWIFT J1842.5-1124	55	6.9	2.2	1.5	7.2	3.8	4.0	1.5	7.2	2.5	1.2	3.0	14
SWIFT J1910.2-0546	73	7.0	1.5	1.1	6.7	3.8	2.9	1.1	6.9	2.5	0.86	2.2	14
XTE J1652-453	40	7.2	5.7	4.1	14	3.8	9.8	3.7	13	2.6	2.8	7.3	25
XTE J1752-223	78	7.1	2.0	1.4	10	3.8	4.4	1.7	11	2.5	1.2	3.0	20
XTE J1810-189	5	7.1	30	21	10	3.9	51	20	8.9	2.6	15	39	17
XTE J1946+274	73	7.0	1.7	1.2	7.7	3.4	4.1	1.4	8.7	2.2	1.6	3.5	22
GX 339-4 (TS)	3	7.2	100	75	18	4.0	190	75	18	2.6	53	140	33
H 1608-522 (TS)	10	7.1	27	19	17	3.9	58	23	20	2.6	18	48	42
IGRJ 17091-3624 (TS)	2	7.3	160	120	23	3.9	330	130	25	2.6	92	240	46
IGRJ 17464-3213 (TS)	8	7.1	19	13	9.4	3.8	32	12	8.7	2.6	8.2	21	15
MAXI J1659-152 (TS)	4	7.1	56	40	15	3.8	120	44	17	2.5	36	91	35
SWIFT J1910.2-0546 (TS)	2	7.1	170	120	18	3.8	370	140	20	2.5	98	250	36
XTE J1652-453 (TS)	49	7.1	3.8	2.7	11	3.8	8.0	3.1	13	2.5	2.4	6.2	26
XTE J1752-223 (TS)	3	7.0	140	97	22	3.8	270	100	23	2.6	68	170	39
			$\cdot 10^{-7}$	$\cdot 10^{-6}$			$\cdot 10^{-7}$	$\cdot 10^{-6}$			$\cdot 10^{-6}$	$\cdot 10^{-6}$	
Units:	[LT] = days | [I(E)] = GeV^2												
	$[\phi_0] = \mathrm{GeV}^{-1}\,\mathrm{cm}^{-2}\,\mathrm{s}^{-1}$ | $[F] = \mathrm{GeV}\,\mathrm{cm}^{-2}\,\mathrm{s}^{-1}$ | $[\mathcal{F}] = \mathrm{GeV}\,\mathrm{cm}^{-2}$										

Table 4. List of jet parameters and neutrino energy flux expected [8] for resolved microquasars, upper limits at 90% C.L. on the neutrino energy fluxes given by ANTARES (F) for a $E^{-2}\exp(-\sqrt{E/100\ \mathrm{TeV}})$ neutrino energy spectra, and upper limits on $\eta_\mathrm{p}/\eta_\mathrm{e}$ resulting from the ANTARES upper limits compared to the expectations [8].

Source	d (kpc)	f (GHz)	S_f (mJy)	l (10^{15} cm)	ψ (deg)	θ (deg)	Γ	$\eta_\mathrm{e}/\eta_\mathrm{p}F_\mathrm{pred}$ (erg s^{-1} cm^{-2})	F U.L. (erg s^{-1} cm^{-2})	$\eta_\mathrm{p}/\eta_\mathrm{e}$ U.L.	Ref.
Cyg X-1	$1.8^{+0.56}_{-0.56}$	8.4	3.1	0.404	< 2	20 – 70	> 1.6	$8.0\ 10^{-12}$ – $1.3\ 10^{-10}$	$1.6\ 10^{-9}$	200	[27]
Cir X-1	7.8 - 10.5	8.4	104	2.3	< 20	0 – 90	> 1	$1.8\ 10^{-11}$ – $1.9\ 10^{-8}$	$1.0\ 10^{-9}$	56	[28]
Cir X-1	$9.4^{+0.8}_{-1.0}$	8.4	104	2.8	< 20	< 3	> 22	$8.2\ 10^{-9}$ – $1.0\ 10^{-5}$	$1.0\ 10^{-9}$	0.1	[23]
H1743-322	$8.5^{+0.8}_{-0.8}$	8.4	6.6	1.72	< 20	75^{+3}_{-3}	1.02 – 1.63	$1.6\ 10^{-12}$ – $2.2\ 10^{-12}$	$8.5\ 10^{-10}$	531	[29, 31]
MAXI J1659-152	7^{+3}_{-3}	5.0	7.3	0.31	< 20	0 – 90	> 1	$6.3\ 10^{-13}$ – $8.2\ 10^{-9}$	$5.2\ 10^{-9}$	8254	[30]

Table 5. List of jet parameters, α_R, $f_{\rm break}$ and $S_{f_{\rm break}}$, neutrino flux energy expected [8] for unresolved microquasars ($\eta_{\rm e}/\eta_{\rm p}F_{\rm pred}$), upper limits on the neutrino energy flux given by ANTARES (F) for $E^{-2}\exp(-\sqrt{E/100\ \rm TeV})$ neutrino energy spectra and upper limits on $\eta_{\rm p}/\eta_{\rm e}$. For GX 339-4, two sets of values, related to two observing periods, are given [32]. For XTE 1752-223 and MAXI J1836-194, the upper limits on $\eta_{\rm p}/\eta_{\rm e}$ are computed assuming $\eta_{\rm e}/\eta_{\rm p}f_\nu$ equal to 1.35 10^{-11} and 9.11 10^{-12} respectively.

Source name	α_R	$\log(f_{\rm break})$ $\log(\rm GHz)$	$S_{f_{\rm break}}$ (mJy)	$\eta_{\rm e}/\eta_{\rm p}F_{\rm pred}$ (erg s^{-1} cm^{-2})	F U.L. (erg s^{-1} cm^{-2})	$\eta_{\rm p}/\eta_{\rm e}$ U.L.
GX 339-4	0.08	$14.26^{+0.12}_{-0.12}$	23^{+18}_{-18}	3.99 10^{-12}	5.0 10^{-10}	125
GX 339-4	0.29	$13.67^{+0.25}_{-0.25}$	251^{+193}_{-193}	1.07 10^{-10}	5.0 10^{-10}	5
XTE 1752-223	0	< 14.26	$6.14^{+5.77}_{-5.77}$	$< 1.35\ 10^{-11}$	2.4 10^{-9}	178
MAXI J1836-194	0	< 13.40	57^{+1}_{-1}	$< 9.11\ 10^{-12}$	2.1 10^{-9}	231